# Characterization of the H3D ASIC Readout System and 6.0 cm$^3$ 3-D Position Sensitive CdZnTe Detectors

Feng Zhang, Cedric Herman, Zhong He, *Senior Member, IEEE*, Gianluigi De Geronimo, Emerson Vernon, and Jack Fried

***Abstract*—Two 20 mm × 20 mm × 15 mm pixelated CZT detectors made by eV-Products were characterized using the new H3D Application Specific Integrated Circuits (ASIC) readout system developed by the Instrumentation Division at Brookhaven National Laboratory. The ASIC is capable of reading out energy and timing signals from 121 anode pixels and the planar cathode electrode of one CZT detector simultaneously. The system has a measured electronic noise of ~2.2 keV FWHM with a dynamic range from 20 keV to 3.0 MeV. The two detectors achieved energy resolution of 0.48% FWHM and 0.60% FWHM, respectively, at 662 keV for single-pixel events from the entire 6.0 cm$^3$ detection volume at room temperature with an un-collimated $^{137}$Cs source. The average $(\mu\tau)_e$ of both detectors were measured to be $>10^{-2}$ cm$^2$/V. The detection efficiency of the two detectors was evaluated at several different energies up to 1.3 MeV by comparing with simulated data. It was found that the total counts agree well between the measured data and the simulated data over the studied energy range. However, the measured photopeak counts were 10–15% lower than simulated photopeak counts at high gamma-ray energies. The analysis shows that the loss of photopeak efficiency is likely due to the charge loss from peripheral pixels to the boundary of detectors.**

***Index Terms*—CdZnTe, position sensitive, 3-D.**

## I. Introduction

WIDE bandgap and high atomic number semiconductors as radiation detectors have been studied for decades, demonstrating high efficiency and excellent energy resolution at room temperature. The most widely studied wide bandgap semiconductor materials (also called room-temperature semiconductors) for gamma-ray detection are CdTe, CdZnTe, $HgI_2$ and TlBr. Among these, cadmium zinc telluride (CdZnTe) is the most promising candidate due to its demonstrated stable operation at large thickness (>1.0 cm), good electron transport properties and commercial availability.

Severe hole trapping has long hindered the application of room-temperature semiconductor detectors. Single-polarity charge sensing techniques, such as coplanar grid electrodes [1] pixelated electrodes [2], and 3-D position-sensing technology [3] were introduced for wide bandgap semiconductor radiation detectors during 1990s. They triggered an intensive development period over the past 15 years on room temperature semiconductor detectors.

Detectors using pixelated electrodes have several advantages. They have smaller leakage current and lower capacitance per pixel electrode, thus lower electronic noise. They are capable of correcting material non-uniformity on the scale of the position resolution, thus more uniform detector response and better energy resolution can be achieved.

3-D position-sensitive semiconductor detectors using pixelated electrodes can also perform gamma-ray imaging. Large volume (>2.0 cm$^3$) 3-D position-sensitive CdZnTe detectors have demonstrated good energy resolution (<1.0% FWHM at 662 keV), position resolution (1–2 mm in x-y and 0.5 mm in z) and uniform detector response [3], [4]. Therefore, these detectors are suitable not only as excellent spectrometers but also as Compton imagers [5]. Energy resolution of ~0.8% FWHM at 662 keV has been demonstrated for several 10 mm thick CdZnTe detectors [4], [6].

However, pixelated detectors require more complicated readout electronics and consume more power. Therefore, it is advantageous to use thicker and larger volume CdZnTe crystals with larger pixels, as the required readout channels and power consumption can be the same as using smaller volume detectors. Also, it is important to improve the ASIC and readout electronics design for lower noise and lower power consumption. This paper presents the latest results for 6.0 cm$^3$ CdZnTe detectors produced by eV-Products that are read out by the BNL-H3D ASIC [7] designed by the Instrumentation Division at Brookhaven National Laboratory.

## II. Detectors and ASIC Readout System

### A. *6.0 cm$^3$ Pixelated CdZnTe Detectors*

Two 20 mm × 20 mm × 15 mm pixelated CdZnTe detectors (cf. Fig. 1(A)) fabricated by eV-Products (the best two from a batch of six such 6.0 cm$^3$ CdZnTe detectors) were used in this study. They are named as #4E-1 and #4E-3, respectively. The 20 mm × 20 mm anode has 11 by 11 pixels with a common grid separating all pixels as shown in Fig. 1(C). The common grid is generally biased at a negative potential relative to the pixels to steer the electrons towards the pixels (so called "steering grid"). The pixel pitch is 1.72 mm and there is a 0.2 mm gap between

Manuscript received March 01, 2011; revised July 11, 2011; accepted October 30, 2011. Date of publication January 04, 2012; date of current version February 10, 2012. The development of CZT detectors and ASIC readout systems were funded by DTRA of the U.S. Department of Defense under Grant DTRA01-02-D-0067. Event reconstruction algorithm development effort was supported by DOE NA-22 Office under Grant DE-FG52-06NA 27499.

F. Zhang and Z. He are with the Department of Nuclear Engineering and Radiological Sciences, University of Michigan, Ann Arbor, MI 48109 USA (e-mail: zhangf@umich.edu).

C. Herman was with the Department of Nuclear Engineering and Radiological Sciences, University of Michigan, Ann Arbor, MI 48109 USA. He is now with Canberra Industries, Inc., Meriden, CT 06450 USA.

G. De Geronimo, E. Vernon, and J. Fried are with the Instrumentation Division at Brookhaven National Laboratory, Upton, NY 11973 USA.

Color versions of one or more of the figures in this paper are available online at http://ieeexplore.ieee.org.

Digital Object Identifier 10.1109/TNS.2011.2175948

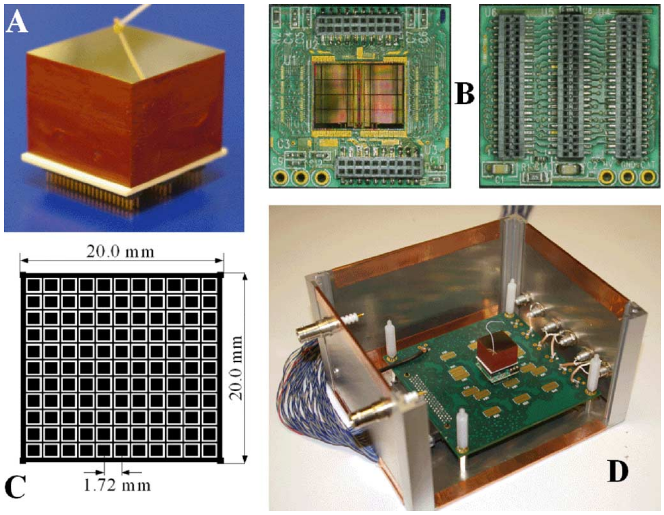


Fig. 1. (A): A 20 mm × 20 mm × 15 mm CdZnTe detector made by eV-Products. (B): The top and bottom views of H3D ASIC front-end board designed by Brookhaven National Laboratory. (C): The common-grid pixelated anode pattern. (D): One assembled detector module mounted on the motherboard.

each pixel and the 0.1 mm wide steering grid. A ceramic substrate with three 42-pin 0.8 mm-pitch pin connectors is bonded to the CdZnTe crystal for signal readout.

The CdZnTe crystals used in these two detectors are single crystals, with neither grain boundary nor twins. They were first fabricated into planar detectors and their responses to an $^{241}$Am source were recorded to make sure that there is no obvious material problem.

## B. *The BNL-H3D ASIC*

The BNL-H3D ASIC was used to read out signals from the detector. Fig. 1(B) shows both sides of the ASIC front-end board. Three 42-pin 0.8-mm pitch sockets, which match the pin connectors on the detector substrate, are mounted on one side of the ASIC front-end board for signal readout.

Each ASIC chip has 124 channels—122 channels (121 were used) for anode pixels ("pixel channels"), 1 channel for the anode grid and 1 channel for the cathode ("cathode channel"). Each channel has a pre-amplifier, baseline stabilizer, shaping amplifier, peak detector, event-triggering, and timing measurement circuits [7].

Fig. 1(D) shows one detector module (detector and ASIC) mounted on a motherboard, which can hold up to nine detector modules.

A readout board (not shown in Fig. 1) is used to control the ASICs and read out their signals. Digitized signals are transmitted to the computer via a USB interface. The ASIC is operated in full readout mode, in which all 124 channels will be read out in series if any pixel is triggered.

# III. Experimental Results

All experiments in this study were performed at room temperatures (varying between 22°C to 26°C in our laboratory) using un-collimated gamma-ray sources. Both detectors were biased at $-3000$ V on the cathode and $-40$ V on the grid. The leakage current between all 121 pixels and the common grid ranged from 80 nA to 100 nA for each detector (less than 1 nA per pixel). The peaking time of the shaping amplifiers on the ASIC was set to 1 $\mu$s for the anode pixels and the cathode.

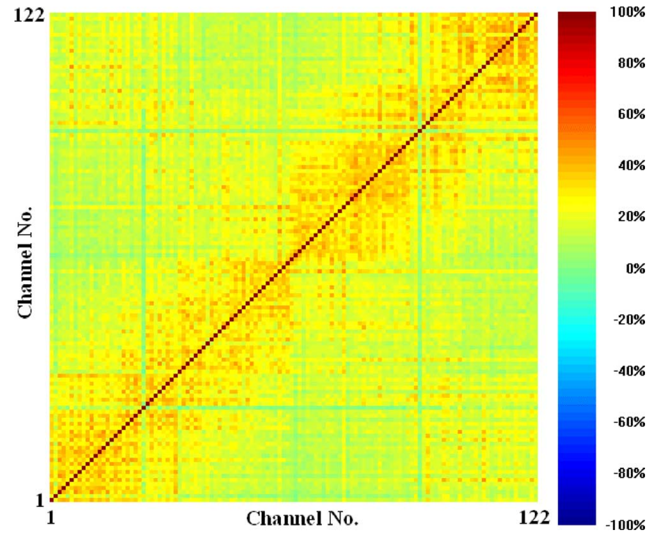


Fig. 2. The correlation between the electronic noise of all pixel channels.

## A. *Electronic Noise and Common-Mode Noise*

The H3D ASIC has on-chip a low noise and high precision test pulse generator, which can be conveniently used to measure the electronic noise. With the detector connected and biased at the high voltage described above, the average electronic noise was measured to be ~2.2 keV FWHM for the pixels and ~5.7 keV FWHM for the cathode.

The correlation of the electronic noise between every pixel channel was calculated and plotted in Fig. 2. A correlation value of 0 between two channels means these two channels have totally independent electronic noise. Any non-zero correlation (either positive or negative) suggests some kind of common-mode noise between two channels. Each channel is naturally 100% correlated with itself. Generally such common-mode noise is caused by signal cross-talk or grounding problems. It can be corrected by baseline deviation averaging and subtraction on event-by-event basis. As shown in Fig. 2, most pixel channels have ~20% correlation with other channels. If not corrected, the average electronic noise for all pixels would be ~2.5 keV FWHM.

## B. *Temperature Variation*

Although relatively stable, the temperature in the lab could still change a few degrees Celsius from day to night. The variations in the $^{137}$Cs 662 keV photopeak centroid and 1-pixel events energy resolution of detector #4E-1 was investigated by breaking the whole 34 hours dataset into sequential subsets of about one million events per subset. Since the photopeak counts in each subset is more than $5 \times 10^4$, the uncertainties in the measured photopeak centroid and the energy resolution are negligible. As can be seen in Fig. 3, the change in the photopeak centroid is less than 0.4 keV and the change in the energy resolution is less than 0.03% FWHM. Therefore, there is no need for

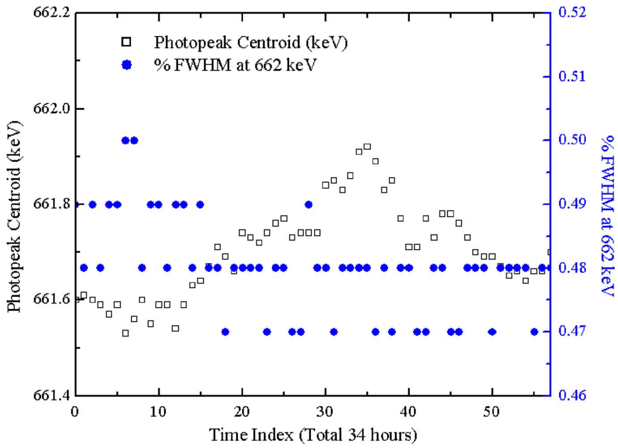


Fig. 3. Variations in the $^{137}$Cs 662 keV photopeak centroid and 1-pixel events energy resolution during 34 hours of data collection for detector #4E-1.

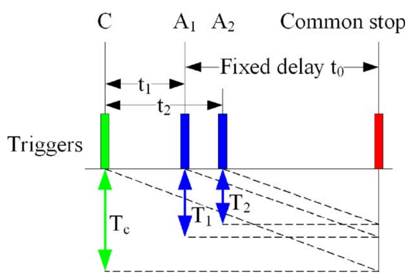


Fig. 4. Illustration of the electron drift time measuring function of the H3D ASIC. The green bar is the cathode trigger, the two blue bars are the triggers from two anode pixels, and the red bar is the common stop signal for the entire ASIC that comes after a fixed delay time following the first pixel trigger.

any special temperature drift calibration if the detector system is used under relatively stable temperature.

### C. Timing Calibration

When electron–hole pairs are created in a pixelated CdZnTe detector and the electrons start to drift towards the anode, the cathode signal immediately starts to rise while the signals on the anode pixels remain insignificant until the electrons move to the vicinity of a pixel. Thanks to this rise time difference in the cathode signal and the anode pixel signals, triggering circuits are designed such that the cathode channel is triggered following the creation of the electron–hole pairs while the anode pixels are triggered when the electrons arrive at the pixels.

The BNL ASIC uses the trigger time differences between the cathode and the pixels to derive the electron drift times for each individual pixel. Each channel (either cathode or pixel) has a Time-to-Amplitude-Converter (TAC). Fig. 4 shows how the timing measurements are done in the BNL ASIC. When one channel has a trigger, its TAC starts a linear voltage ramp whose amplitude is proportional to the time between the trigger and a common stop signal. The readout system is triggered by the first trigger from any pixel. After a preset fixed delay time (a few $\mu$s, to allow multiple interactions to arrive at the anode pixels at different times), a common stop signal is sent to all channels.

The timing signals for a typical 2-pixel event depicted in Fig. 4 are shown in (1) below, where $T_c, T_1$ and $T_2$ are the timing signals of the cathode and the two pixels, $G_c, G_1$ and $G_2$ are the gains of timing circuitries of the cathode and the two pixels, $t_0$ is the preset fixed delay time, $t_1$ and $t_2$ are the electron drift times for the two pixels.

$$\begin{aligned} T_c &= (t_0 + t_1) \times G_c \\ T_1 &= t_0 \times G_1 \\ T_2 &= (t_0 + t_1 - t_2) \times G_2 \end{aligned} \tag{1}$$

Therefore, in order to derive the electron drift times $t_1$ and $t_2$ from the readout timing signals $T_c, T_1$ and $T_2$, the timing gains ($G_c, G_1, G_2$, etc.) of the cathode channels and all pixel channels need to be calibrated, as can be seen from (2).

$$\begin{aligned} t_1 &= \frac{T_c}{G_c} - \frac{T_1}{G_1} \\ t_2 &= \frac{T_c}{G_c} - \frac{T_2}{G_2} \end{aligned} \tag{2}$$

An automatic timing calibration program has been implemented for the BNL ASIC readout system. An internal test pulse is injected into all channels simultaneously. By changing the system trigger-hold delay time $t_0$ and measuring the changes in the output timing signals of each channel, the timing gain coefficients of all channels can be quickly calibrated. The calibrated timing gain coefficients can then be used to convert raw timing signals into a value in nanoseconds, which can then be used to get the true time difference (in ns) between the cathode trigger and each individual pixel trigger. This is the electron drift time.

### D. Spectroscopic Performance

The energy resolution of 1-pixel events, 2-pixel events, 3-pixel events, 4-pixel events, and all events (in which any number of pixels triggered) for detector #4E-1 and #4E-3 are listed in Table I. In these results, there is no preferential selection of "good" events or discarding of "bad" events; all collected events are included. Thanks to the low noise BNL ASIC, detector #4E-1 achieved an energy resolution of 0.48% FWHM at 662 keV for 1-pixel events (~30% of all 662 keV full energy peak events). Even with all events included, the energy resolution of 0.71% FWHM at 662 keV achieved by detector #4E-1 is still very good for a 6.0 cm$^3$ CdZnTe detector.

TABLE I
ENERGY RESOLUTION (FWHM) AT 662 KEV

| | 1-pixel events | 2-pixel events | 3-pixel events | 4-pixel events | All events |
|---|---|---|---|---|---|
| #4E-1 | 0.48% | 0.89% | 1.23% | 1.68% | 0.71% |
| #4E-3 | 0.60% | 0.99% | 1.35% | 1.77% | 0.84% |

Multiple-pixel events have worse energy resolution than 1-pixel events; the more pixels trigger, the worse is the resolution. This is partly due to the added electronic noises when adding more signals together. Other factors, such as worse timing resolution at lower energies, non-linearity, and signal cross-talk between pixels and their readout electronics, can all contribute to the resolution degradation of multiple-pixel events.

Fig. 5(A) shows the 3-D corrected $^{137}$Cs spectrum and the pixel map of energy resolution of 1-pixel events from detector

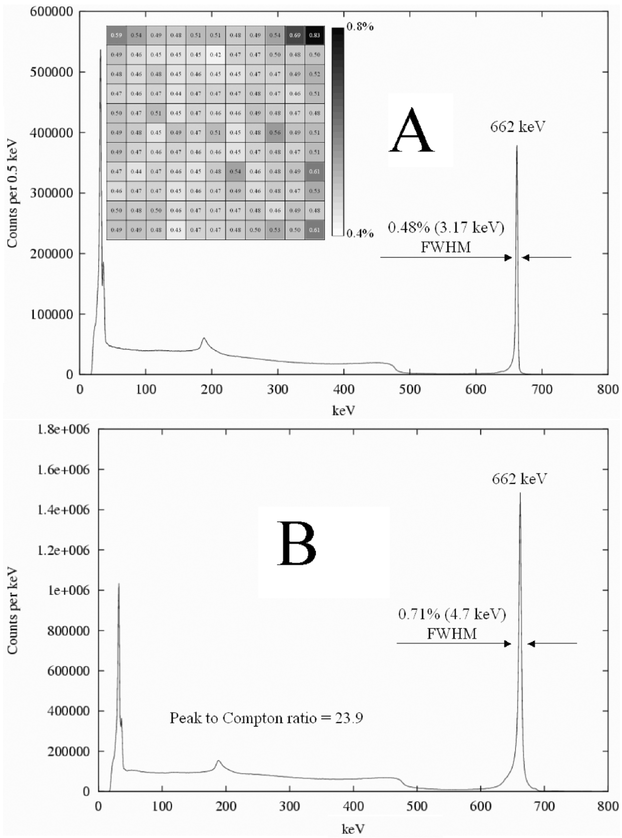


Fig. 5. 3-D corrected $^{137}$Cs spectra collected from detector #4E-1 biased at $-3000$ V on the cathode and $-40$ V on the grid. (A). Spectrum for 1-pixel events. The inset shows energy resolution (% FWHM) at 662 keV for each pixel. (B). Spectrum for all events (1-pixel, 2-pixel, etc.).

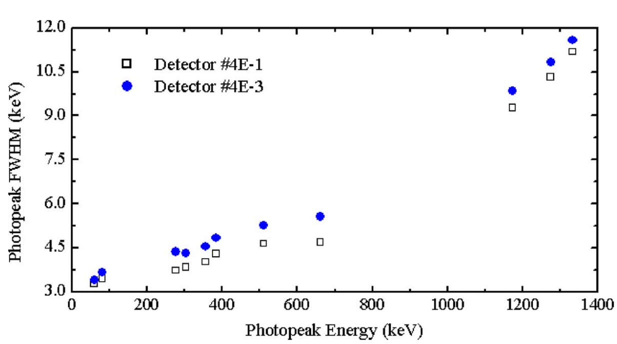


Fig. 6. Energy resolutions at different energies for all events collected from detector #4E-1 and #4E-3. $^{241}$Am, $^{133}$Ba, $^{137}$Cs, $^{22}$Na and $^{60}$Co sources were used.

#4E-1. The 32 keV and 36 keV x-ray peaks from the $^{137}$Cs source are both visible and clearly separated in the spectrum. The corrected $^{137}$Cs spectrum of all events for detector #4E-1 is shown in Fig. 5(B), in which a peak-to-Compton ratio of $\sim$24 is achieved. Fig. 6 shows energy resolutions for all events (any-number-of-pixel events) at different energies obtained by irradiating the detectors from the cathode side using several common gamma-ray sources—$^{241}$Am, $^{133}$Ba, $^{137}$Cs, $^{22}$Na and $^{60}$Co. The energy resolution gets worse at higher energy since the fraction of resolution-degrading multiple-pixel events increases at higher energies.

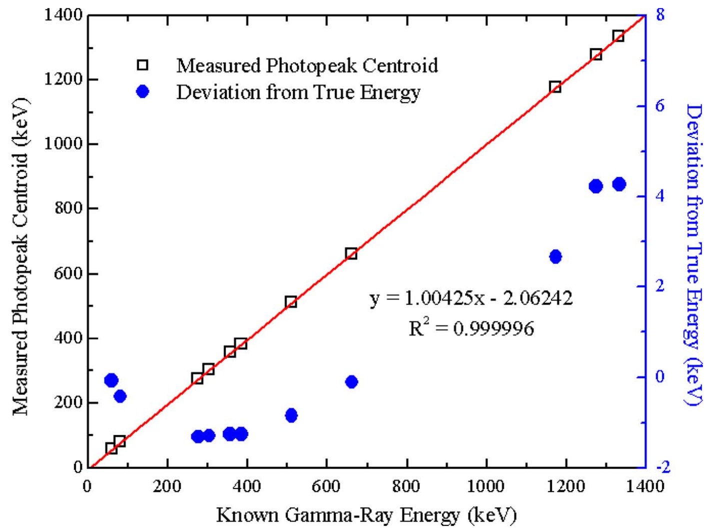


Fig. 7. Relation between the measured photopeak centroid energy and the true energy for 1-pixel events collected from detector #4E-1.

## E. Linearity

An $^{241}$Am source and a $^{137}$Cs source were used for a pixel-by-pixel baseline offset calibration and the 3-D position-dependent calibration. The linearity of the system (the detector together with the ASIC electronics) was then calibrated using several common gamma-ray sources, as shown in Fig. 7. Though from the linear-fitting it seems the system is very linear, the measured photopeak can still deviate from the true energy by a few keV. It is not surprising to see that the measured photopeak energy matches exactly with the true energy at 59.5 keV and 662 keV since the system was calibrated at these two energies. The non-linearity is small ($\sim$1 keV deficit) between 59.5 keV and 662 keV but gets larger above 1 MeV ($\sim$4 keV deviation at 1.3 MeV, $\sim -0.3\%$). Such non-linearity must be calibrated otherwise it will degrade the energy resolution of multiple-pixel events.

## F. Electron Mobility-Lifetime Products

Energy spectra for $^{137}$Cs 1-pixel events occurring on the cathode side were collected for each pixel under two different cathode biases. Events interacting near the cathode were identified by using the interaction depths derived from the electron drift times. The electron mobility lifetime product can be calculated (3) described by Z. He *et al.* [8]

$$(\mu\tau)_e = \frac{D^2}{\ln\left(\frac{H_{a1}}{H_{a2}}\right)}\left(\frac{1}{V_2} - \frac{1}{V_1}\right) \tag{3}$$

in which $D$ is the detector thickness (1.5 cm), and $H_{a1}$ and $H_{a2}$ are the measured photopeak centroids for cathode side events under two different cathode biases, $V_1$ and $V_2$. The measured $(\mu\tau)_e$ for each pixel is shown in Fig. 8.

Detector #4E-1 has an average $(\mu\tau)_e$ of $1.61 \times 10^{-2}$ cm$^2$/V with a standard deviation of $0.04 \times 10^{-2}$ cm$^2$/V. Detector #4E-3 has an average $(\mu\tau)_e$ of $1.09 \times 10^{-2}$ cm$^2$/V with a standard deviation of $0.03 \times 10^{-2}$ cm$^2$/V. The error in the $(\mu\tau)_e$ measurements is mainly due to the uncertainty in the interaction depth

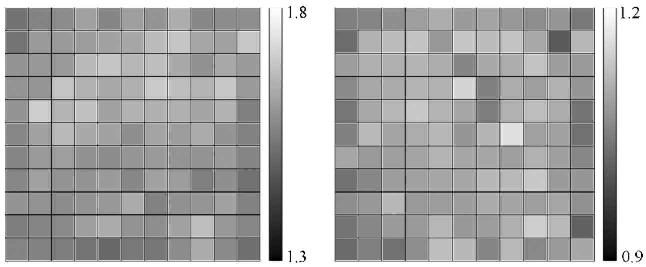


Fig. 8. Pixel maps of measured $(\mu\tau)_e$ for detector #4E-1 (left) and #4E-3 (right). The unit for the values shown in the figures is $10^{-2}$ cm$^2$/V.

TABLE II
ACTIVITY OF THE GAMMA-RAY SOURCES USED IN THIS STUDY

| | $^{241}$Am | $^{137}$Cs | $^{60}$Co |
|---|---|---|---|
| Activity (µCi) | 9.79 | 6.52 | 2.32 |
| Uncertainty | ±4% | ±4% | ±3% |

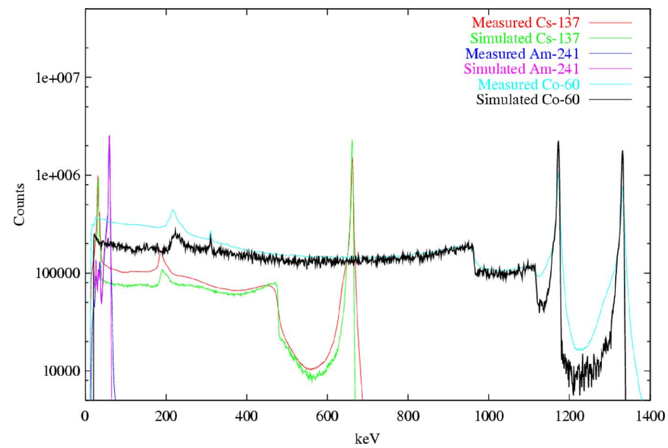


Fig. 9. Measured spectra (detector #4E-1) and simulated spectra for $^{137}$Cs, $^{241}$Am and $^{60}$Co gamma-ray sources, respectively. The heights of the simulated spectra are normalized to their corresponding measured spectra according to the measurement time, source activity and total simulated events.

derived from the electron drift time, which should be less than 5%.

## IV. Detection Efficiency

Excellent energy resolution has been achieved with two 6.0 cm$^3$ 3-D position sensitive CdZnTe detectors as presented in Section III. However, it is unclear whether the entire volume of each detector is fully active or whether there is any efficiency loss due to material defects and incomplete charge collection. In this section, the detection efficiency of 3-D position-sensitive CdZnTe detectors at several benchmark energies is analyzed by comparing the experimental results to Geant4 [9] simulation results.

### A. Experimental Setup

Detector #4E-1 and #4E-3 were used in this efficiency study. The triggering threshold of the system was set to approximately 25 keV for all 121 pixels. The actual triggering threshold could vary $\pm 5$ keV from pixel to pixel due to non-uniform ASIC response. Since all pixels are read out for each event, a software threshold is used to determine which pixels have true signal and which pixels have only noise. A software threshold of $\sim$20 keV was used in the experiment.

Data from $^{241}$Am, $^{137}$Cs and $^{60}$Co sources (their activities at the time of this experiment are listed in Table II) were collected for both detectors. Background data was also collected and subtracted from the experimental data for each source.

The readout dead time of the BNL_H3D ASIC was measured to be $\sim$190 $(\pm 1)$ $\mu$s. It was used to normalize the measured counts before comparing to the simulated counts.

### B. Simulation

The simulation was done using Geant 4.9.1 [9]. A simplified geometry close to the one shown in Fig. 1(D) was modeled—an aluminum box (1.0-mm thick walls), one high voltage supply board, one motherboard, and the detector. The gamma-ray point sources were placed 5.2 cm above the cathode of the detector.

The following physical processes were implemented in the simulation model:

1) Tracking of the electron ionization process and energy deposition along the track.
2) Electron cloud diffusion.
3) Weighting potential along the centerline of the collecting pixel.
4) 11 × 11 pixels to collect deposited energy.
5) $\sim$2.2 keV FWHM Gaussian noise added to the collected energy for each pixel.
6) A 25 keV triggering threshold.
7) A 20 keV software threshold to determine whether a pixel has real signal or just noise.

The physical processes listed below are much more complicated to implement in the simulation model but are related to the energy resolution rather than the efficiency. Therefore, they were not included in the simulation model:

1) Lateral variation of weighting potential and non-collecting pixel weighting potential.
2) The actual electric field inside the detector and the actual electron drift trajectory.
3) Electron/hole trapping.
4) Waveform generation, pulse shaping, triggering and timing.

### C. Results and Discussion

Measured and simulated spectra of the three gamma-ray sources are shown in Fig. 9 for detector #4E-1. The heights of the simulated spectra are normalized to their corresponding measured spectra according to the measurement time, source activity and total simulated events. All spectra of three sources are scaled in heights to be shown in the same figure for better comparison. The intrinsic efficiency of the detector for the simulated geometry is 98.9% at 59.5 keV ($^{241}$Am), 11.2% at 662 keV ($^{137}$Cs), and 4.4% at 1.33 MeV ($^{60}$Co), respectively.

Table III presents the comparison between the measured results and the simulated results for all 121 pixels in different energy ranges. The ratio of the measured counts and the simulated counts should be 1.0 if they exactly match. As can be seen in Fig. 9, the shoulder below and above the photopeak (exaggerated due to the log scale) in the measured spectra are mostly

TABLE III
COMPARISON OF MEASURED AND SIMULATED RESULTS OF TOTAL COUNTS AND PHOTOPEAK COUNTS FOR THE TWO DETECTORS AT DIFFERENT GAMMA-RAY ENERGIES. EVENTS FROM ALL 121 PIXELS ARE CONSIDERED

| Source | Energy range (keV) | | Detector #4E-1 (Measured counts / Simulated counts) | Detector #4E-3 (Measured counts / Simulated counts) |
|---|---|---|---|---|
| $^{241}$Am | Photopeak | 50 – 70 | 0.97 ± 0.04 | 0.97 ± 0.04 |
| $^{137}$Cs | Total | 0 – 800 | 1.01 ± 0.04 | 1.02 ± 0.04 |
| | Photopeak | 20 – 40 | 0.96 ± 0.04 | 0.96 ± 0.04 |
| | Photopeak | 550 – 700 | 0.87 ± 0.04 | 0.90 ± 0.04 |
| $^{60}$Co | Total | 0 – 1400 | 0.96 ± 0.03 | 0.94 ± 0.03 |
| | Photopeak | 1120 – 1230 | 0.82 ± 0.03 | 0.86 ± 0.03 |
| | Photopeak | 1230 – 1400 | 0.81 ± 0.03 | 0.85 ± 0.03 |

TABLE IV
COMPARISON OF MEASURED AND SIMULATED RESULTS OF TOTAL COUNTS AND PHOTOPEAK COUNTS FOR THE TWO DETECTORS AT DIFFERENT GAMMA-RAY ENERGIES. ONLY EVENTS IN THE CENTRAL 9 × 9 PIXELS ARE CONSIDERED

| Source | Energy range (keV) | | Detector #4E-1 (Measured counts / Simulated counts) | Detector #4E-3 (Measured counts / Simulated counts) |
|---|---|---|---|---|
| $^{241}$Am | Photopeak | 50 – 70 | 1.08 ± 0.04 | 1.04 ± 0.04 |
| $^{137}$Cs | Total | 0 – 800 | 1.05 ± 0.04 | 1.03 ± 0.04 |
| | Photopeak | 20 – 40 | 1.01 ± 0.04 | 1.02 ± 0.04 |
| | Photopeak | 550 – 700 | 1.01 ± 0.04 | 0.99 ± 0.04 |
| $^{60}$Co | Total | 0 – 1400 | 1.01 ± 0.03 | 1.00 ± 0.03 |
| | Photopeak | 1120 – 1230 | 0.95 ± 0.03 | 0.97 ± 0.03 |
| | Photopeak | 1230 – 1400 | 0.95 ± 0.03 | 0.96 ± 0.03 |

due to material non-uniformity, charge collection problem and improper calibrations, which are not modeled in this simulation. Therefore, fairly wide energy windows around the photopeaks were used to make sure the simplified model in the simulation would not affect the results. The uncertainties in the calculated ratio values are dominated by the uncertainties in the gamma-ray source activity shown in Table II.

For the $^{241}$Am source, the measured photopeak counts match very well with the simulated counts. For high-energy gamma rays, the total counts agree well between the measured counts and the simulated counts. However, there is a 10% to 15% loss of measured photopeak counts at 662 keV and 15% to 20% loss at 1.3 MeV. Because the total counts agree well for both detectors, the "lost" photopeak counts must by some reason end up in the Compton continuum. Therefore, the "lost" photopeak counts are very likely due to incomplete charge collection (thus lower signal amplitude and falling out of the peak region but still contributing to the total counts).

The region near the anode pixels (so called "dead layer") could be where the photopeak events are lost due to the steep change in the weighting potential and thus much smaller signal contribution from the electrons. However, since the weighting potential of the collecting pixel was already modeled in the simulation, this "dead" layer ($\sim$1 mm thick) near the anode should have already been taken into account. Even this "dead" layer (for electrons) is not completely dead since the holes can instead contribute to the signal due to the steep change in the weighting potential. Indeed our study using collimated gamma-ray beams estimates this "dead" layer to be less than 0.3 mm thick.

Another possibility is that some electrons may be lost to the gap or the steering grid (so called "insufficient steering effect"). However, the data showed that side-neighboring 2-pixel events (many of which are actually 1-interaction charge-sharing events, and are most susceptible to charge loss due to poor steering) with a centroid depth close to the cathode, such that there is no signal deficit due to the immobile holes, have a photopeak centroid exactly at 662 keV. This suggests that there is no appreciable charge loss to the grid or gap.

A more probable region for the loss of photopeak efficiency is the peripheral region (outmost guard-ring) of the detector. There may be incomplete charge collection underneath the guard-ring, electron loss to the side surface due to distorted electric field near the side surface, or charge sharing between the guard ring and the peripheral pixels. To prove this is the case, the measured data and the simulated data were re-processed with all events involving 40 peripheral pixels excluded. The results for the central 9 × 9 pixels are shown in Table IV. The photopeak counts agree much better at 662 keV for the inner 81 pixels, though there is still 3% to 5% deficit at 1.3 MeV probably due to underestimated electron cloud size, charge repulsion and diffusion in the simulation.

Reducing the width of the guard ring could reduce this loss of photopeak efficiency, or the guard ring could be placed on the side surface. We will also work with the detector vendor to study how to process the side surface so that the electric field near the side surface will steer the electrons towards the center of the detector instead of attracting the electrons to be trapped on the side surface.

## V. SUMMARY

Two 6.0 cm$^3$ CdZnTe detectors were evaluated using the new BNL-H3D ASIC readout system. Both the detectors and the ASIC worked well as designed and achieved good performance.

With the detectors mounted and biased, the electronic noise of the ASIC was measured to be only 2.2 keV FWHM after common-mode noise rejection. As a result, the two detectors achieved 0.48% FWHM and 0.60% FWHM at 662 keV for all 1-pixel events, respectively, after 3-D detector response calibration and correction. When all events are included (1-pixel events, 2-pixel events, 3-pixel events, 4-pixel events, etc.), the two detectors achieved 0.71% FWHM and 0.84% FWHM at 662 keV, respectively. Both detectors have very high $(\mu\tau)_e$—one is $1.6 \times 10^{-2}$ cm$^2$/V and the other is $1.1 \times 10^{-2}$ cm$^2$/V, which is another reason why they achieved excellent energy resolution.

The active detection volume of the two detectors was investigated by comparing experimentally measured counts to simulated counts for the same geometry and source activities. It was found that the measured and simulated total counts match within the uncertainty of the source activities. However, the measured photopeak counts at energies above 1 MeV is 10% to 20% less than the simulated photopeak counts for the entire detector. Further analysis showed that this loss of photopeak efficiency is very likely due to the charge loss from peripheral pixels to the boundary of the detector. Such charge loss could be improved by using a narrower boundary grid, or by moving the boundary grid to the side of the detector, or by passivating the side surface of the detector in some way to form an inward-steering electric field.

The results presented in this paper proved that the energy resolution of 3-D position sensitive CdZnTe detectors does not necessarily degrade with increasing detector volume/thickness. Although the yield of these large volume high quality CdZnTe detectors is low, the excellent energy resolution from these two detectors suggest that it is possible to produce large volume CdZnTe detectors that can approach the theoretical limit of energy resolution for CdZnTe detectors ($\sim$0.2% FWHM at 662 keV) with the help of low noise readout electronics and specialized calibration and correction algorithms.

## REFERENCES

[1] P. N. Luke, "Single-polarity charge sensing in ionization detectors using coplanar electrodes," *Appl. Phys. Lett.*, vol. 65, no. 22, pp. 2884–2886, 1994.

[2] H. H. Barrett, J. D. Eskin, and H. B. Barber, "Charge transport in arrays of semiconductor gamma-ray detectors," *Phys. Rev. Lett.*, vol. 75, no. 1, pp. 156–159, 1995.

[3] Z. He *et al.*, "3-D position sensitive CdZnTe gamma-ray spectrometers," *Nucl. Instrum. Meth. A*, vol. 422, no. 1–3, pp. 173–178, 1999.

[4] F. Zhang *et al.*, "3D position sensitive CdZnTe spectrometer performance using third generation VAS/TAT readout electronics," *IEEE Trans. Nucl. Sci.*, vol. 52, no. 5, pp. 2009–2016, Oct. 2005.

[5] C. E. Lehner, Z. He, and F. Zhang, "$4\pi$ compton imaging using a 3-D position-sensitive CdZnTe detector via weighted list-mode maximum likelihood," *IEEE Trans. Nucl. Sci.*, vol. 51, no. 4, pp. 1618–1624, Aug. 2004.

[6] F. Zhang, Z. He, and C. E. Seifert, "A prototype three-dimensional position sensitive CdZnTe detector array," *IEEE Trans. Nucl. Sci.*, vol. 54, no. 4, pp. 843–848, Aug. 2007.

[7] G. De Geronimo *et al.*, "Readout ASIC for 3-D position-sensitive detectors," *IEEE Trans. Nucl. Sci.*, vol. 55, no. 3, pp. 1593–1603, Jun. 2008.

[8] Z. He, G. F. Knoll, and D. K. Wehe, "Direct measurement of product of the electron mobility and mean free drift time of CdZnTe semiconductors using position sensitive single polarity charge sensing detectors," *J. Appl. Phys.*, vol. 84, no. 10, pp. 5566–5569, 1998.

[9] S. Agostinelli *et al.*, "Geant4—A simulation toolkit," *Nucl. Instrum. Meth. A*, vol. 506, pp. 250–303, 2003.